Journal of
Materials Chemistry A

ROYAL SOCIETY
OF CHEMISTRY

PAPER

View Article Online
View Journal

Check for updates

Cite this: DOI: 10.1039/d6ta02098d

Mixed-anion electrolytes: from bulk speciation to interfacial dynamics in divalent metal electrodeposition

Zhenzhen Yang,*[abc] Stefan Ilic,[bd] Qian Liu,[c] Chen Liao,[bc] Lynn Trahey[b] and Brian J. Ingram*[abc]

Received 10th March 2026
Accepted 9th May 2026

DOI: 10.1039/d6ta02098d

rsc.li/materials-a

Mixing anions is emerging as a promising strategy for multivalent electrolyte design, allowing for adjustment of the solvation structure of bulk cations and enhancing the efficiency of electrochemical processes (*e.g.* metal deposition for batteries and catalysis). Further progress in electrolyte development requires a fundamental understanding of how tailored electrolyte speciation in mixed anion systems can modify the dynamic electrochemical interface during metal cycling. In this study, we present an anode-focused mechanistic study of exemplar Mg electrolytes containing three different secondary anions, correlating electrochemical behavior with bulk speciation and *operando* interfacial dynamics. Electrospray Ionization-Mass Spectrometry (ESI-MS) results reveal a general trend of forming mixed anion contact ion pairs (CIPs) across various anions, with the extent of ion pairing influenced by the association strength of the secondary anion. *Operando* multiharmonic electrochemical quartz crystal microbalance with dissipation (EQCM-D) reveals how these bulk species influence interfacial mass uptake, viscoelasticity, and solvent-coupled hydrodynamic behavior during deposition and stripping. The results indicate that Mg-containing ion pairs and solvated complexes shape adsorption, nucleation, and deposit growth, leading to distinct anion-dependent interphases ranging from more permeable, solvent-coupled layers to relatively compact and rigid deposits. This work establishes a quantitative link between bulk speciation and interfacial dynamics in divalent metal electrodeposition and provides mechanistic guidance for electrolyte design.

1. Introduction

Metal electrodeposition processes are essential for various applications and are fundamental to advancements in electrochemical energy storage, electrorefining, electronics, corrosion protection, and beyond. In the field of energy storage, systems utilizing earth-abundant elements present a promising path for advancing battery technology and enhancing energy efficiency. Current research focuses on cost-effective batteries such as magnesium (Mg),[1,2] zinc (Zn),[3] iron (Fe),[4,5] and calcium (Ca),[6] which are crucial for establishing a robust economic foundation and integrating storage technology with a robust material supply chain. In multivalent systems, however, electrolyte design remains a central challenge because electrolyte composition governs not only bulk cation speciation, but also interfacial compatibility, deposition/stripping behavior, and the evolution of passivation layers at metal electrodes. Developing electrolytes that combine a wide electrochemical window with stable, reversible metal-electrode operation is therefore critical for both fundamental understanding and practical implementation.[7]

Extensive fundamental research suggests that electrolyte speciation strongly influences electrochemical behavior, by regulating the bulk transport characteristics of the electrolyte and the electrode–electrolyte interface during electrodeposition. The precise electrolyte composition critically determines electrolyte species and solvation structures, resulting from complex cation–solvent, cation–anion, and solvent–solvent interactions.[8,9] Anion chemistry and composition directly impact ion pairing in solvation processes; they are essential for determining the mechanisms and kinetics of reactions.[10] Bis(trifluoromethane sulfonyl)imide ($TFSI^-$), a benchmark anion for most Mg, Zn, and Ca batteries, has desirable characteristics for applications, such as excellent thermal stability, high solubility in ethers, and good oxidation stability.[7,11] However, these "simple" solutions have poor electrochemical performance for processes involving the deposition and dissolution of metals, with low coulombic efficiency and significant hysteresis.[2]

---

[a] *Center for Steel Electrification by Electrosynthesis, Argonne National Laboratory, Lemont, IL 60439, USA. E-mail: yangzhzh@anl.gov; Ingram@anl.gov*
[b] *Joint Center for Energy Storage Research, Lemont, IL 60439, USA*
[c] *Chemical Sciences and Engineering Division, Argonne National Laboratory, Lemont, IL 60439, USA*
[d] *Material Science Division, Argonne National Laboratory, Lemont, Illinois 60439, USA*

To improve reversible redox processes at the metal anode, multivalent electrolytes developed thus far rely on the addition of a second strongly coordinating anion (*e.g.*, halide anions such as Cl^-, Br^-, and I^-).[12–14] This cooperative effect arises from variations in the strength of the TFSI–cation and halide–cation complex associations. For example, introducing high concentrations of chloride (Cl^-) enables engineering and reorganization of the first solvation shell by forming contact ion pairs (CIPs) with isolated $TFSI^-$ anions in the electrolyte bulk.[12] The modified solvation sheath exhibits lower polarization effects at the anode/electrolyte interface. As a result, the dual-salt electrolyte effectively reduces parasitic reactions by limiting the solvent decomposition and enhancing the reversibility of Mg/Zn/Ca-based electrochemical systems.[14,15] Nevertheless, these systems are not compatible with oxide cathodes for practical high-voltage multivalent batteries because of their poor anodic stability, resulting in electrode corrosion. Therefore, recent studies have focused on using non-corrosive anions to leverage co-anion effects and surpass the performance of current single-anion electrolytes. $Mg(BH_4)_2$ or $Ca(BH_4)_2$ was introduced as a co-anion to regulate coordination interaction between TFSI and Mg^{2+} /or Ca^{2+} in the electrolyte.[16–18] Similar findings were found for HMDS, and trifluoromethanesulfonate (triflate, OTf^-) emerges as a remarkable co-anion with an improved solvation structure and electrochemical performance with a marked reduction in overpotential for Mg plating.[19–21]

While recent findings highlight the potential of tailored electrolyte co-anions to modify solvation coordination, the challenge remains to develop general design guidelines accounting for the unique properties of each electrolyte, their complex coordination, and their impact on interfacial structure and functionality. The highly dynamic nature of the interface and the limitations of real-time experimental methods have left the role of bulk electroactive species in interface reactions largely unexplored. For instance, the electrolyte structure at the interface, particularly in the double layer, differs from that in the bulk due to selective ionic adsorption, and this difference becomes more pronounced during electrochemical processes at the polarized interface. In this work, we established $Mg(TFSI)_2$/diglyme (G2) as an exemplar system to investigate the relationship between solvated bulk structures and interfacial dynamics during Mg plating in various mixed-anion electrolytes. We selected three co-anions—BH_4^-, $HMDS^-$, and OTf^-—spanning a wide spectrum of properties, from the small, hard BH_4^- to the bulky, soft $HMDS^-$, to create distinct ion-pairing environments to test their direct impact on the electrodeposition process. Using Electrospray Ionization-Mass Spectrometry (ESI-MS), we then systematically identified and quantified the stable solvation species in these systems. Electrochemical metal plating and stripping involve intricate, multistep reactions at the electrode/electrolyte interface, occurring over time scales from milliseconds to hours and length scales from nanometers to micrometers. To probe the evolving electrochemical interface beyond bulk speciation, we employed a highly sensitive *operando* multiharmonic electrochemical quartz crystal microbalance with dissipation (EQCM-D) to monitor interfacial reactions in real time.[22–26] This technique provides quantitative information on interfacial mass, viscoelasticity, and solvent-coupled hydrodynamic behavior during metal deposition. By integrating ESI-MS with *operando* EQCM-D, we correlate mixed-anion bulk speciation with dynamic interfacial behavior and show how anion chemistry governs nucleation, deposit growth, and deposition efficiency. Additionally, the quantitative technique combined ESI-MS/EQCM-D approach provides a general experimental strategy for studying coupled electrolyte effects in metal electrodeposition and related electrochemical systems.

2. Results and discussion

2.1 Effect of mixed anions on the electrochemistry of Mg plating/stripping

Fig. 1a shows the structure and variation in the anion association strength trend predicted from previous DFT calculations with Mg^{2+} from the literature.[15,27] Due to their size (steric hindrance), charge density, electronegativity and polarizability, the coordinating ability with Mg^{2+} increases in the order $HMDS^- < BH_4^- < TFSI^- < OTf^- < Cl^-$. Based on this evidence, 0.25 M $Mg(X)_2$ was mixed with 0.25 M $Mg(TFSI)_2$ (1 : 1 ratio for TFSI : X), resulting in a total Mg^{2+} concentration of 0.5 M (baseline with TFSI-only) to compare the co-anion effect on the electrolyte performance in this work. The initial electrochemical performance of various mixed anion electrolytes was evaluated by cyclic voltammetry (CV) cycling on a fresh Pt electrode, as shown in Fig. 1b and c. Compared to the baseline in Fig. 1b, the widely employed $MgCl_2$ dual-salt by the community shows much improved performance in terms of coulombic efficiency (CE) and reduced overpotential for Mg plating and stripping (defined as the onset peak at plating/stripping current densities of ±1 mA cm^{-2}). CV curves in Fig. 1c compare the non-halide co-anion systems. Two major differences in Mg redox behavior are clearly observed. First, the co-anion electrolyte containing either BH_4 or OTf exhibits higher current density, indicating a greater concentration of Mg^{2+} charged species available for the redox reaction. Second, these co-anions considerably lower the onset potential for the stripping peak, from 1724 mV to <300 mV for the co-anion systems. Between HMDS and OTf, a similar overpotential of 277 mV was seen. A second, smaller stripping peak is also observed at a higher overpotential for HMDS and OTf, which can be attributed to Mg dissolution from regions covered by a thicker or more resistive passivation layer on the electrode surface. Unlike lithium systems, the SEI on Mg is often non-uniform and can obstruct cation migration, resulting in stripping events at distinctly different potentials depending on the local interfacial resistance.[28] Overall, their performance aligns well with their coordinating strength. Notably, the OTf electrolyte demonstrates the highest apparent coulombic efficiency (86%) among the three anion candidates and is comparable to the one with $MgCl_2$.

Using a three-electrode configuration for these electrolytes, the reversible cycling performance of Mg deposition and dissolution was further examined in galvanostatic Mg||Mg symmetric cells at a current density of 0.5 mA cm^{-2}. As shown in Fig. 1d, several preconditioning cycles were necessary to activate

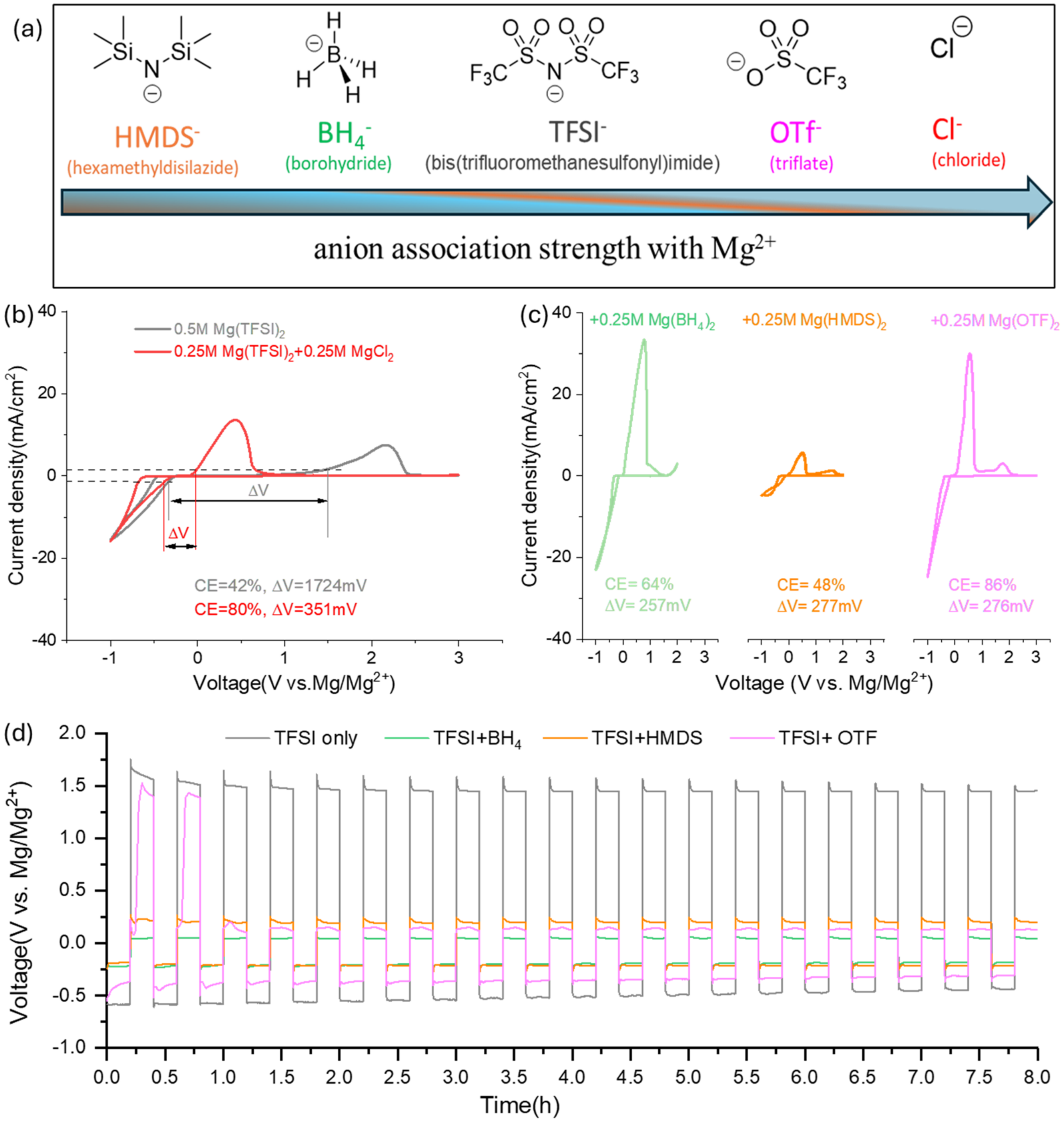

Fig. 1 (a) Chemical structures of various anions and the predicted trend in their association strength with Mg^{2+}, as determined by previous DFT calculations from the literature. (b) Initial evaluation of Mg plating/stripping performance was conducted using cyclic voltammograms (CVs) with different electrolytes on a Pt disk electrode in a three-electrode system cell: 0.5 M $Mg(TFIS)_2$ baseline and addition of the commonly used $MgCl_2$ for comparison; (c) effect of mixed anions including $Mg(BH_4)_2$, $Mg(HMDS)_2$ and $Mg(OTf)_2$ on TFSI-electrochemistry. The scan rate was set at 25 mV s^{-1}. A 2.0 V cut-off was applied during the anodic polarization steps to prevent BH_4^- oxidation, which starts at voltages greater than 2 V *vs.* Mg/Mg^{2+}. (d) Galvanostatic cycling of a Mg||Mg symmetric cell in a three-electrode configuration with dual-salt electrolytes at a current density of 0.5 mA cm^{-2} for a charge capacity of 0.1 mA h cm^{-2}.

the effective interfacial reactions, which is a common requirement in magnesium batteries. This is reflected by the voltage fluctuations observed during the initial cycles, originating from the dynamic breakdown and reformation of the surface passivation layer, particularly in the presence of trace impurities in the electrolyte and the native oxide layer on the magnesium metal anode.[29,30] The cell's overpotential for Mg plating/stripping decreases over the first six cycles as the electrolyte and electrode surface become cleaner, eventually leading to stabilized cell polarization. After 2 h cycling, the $V_{plating}$ at −0.5 V of Mg cycled in the baseline increases to −0.35 V for OTf, −0.21 V for BH_4 and HMDS. While the TFSI baseline remains high at 1.5 V, $V_{stripping}$ for BH_4, HMDS, and OTf decreases to 0.06 V, 0.24 V, and 0.14 V, respectively. The overpotentials observed during the stripping process are closely related to the passivation of the magnesium interface due to various parasitic electrolyte reduction mechanisms.[31,32]

2.2 Bulk speciation

We then employed ESI-MS to characterize how the distinct chemistry and ion-pairing tendencies of these co-anions modulate the Mg^{2+} speciation in the bulk electrolyte. The positive and negative modes of ESI-MS spectra are shown in Fig. 2a and b, respectively. Due to the presence of solvated species in the solution undergoing a series of equilibria, various solvate species and complexes can coexist simultaneously. Table 1 summarizes the relative ratio of the major ionic species, characterized by fully or under-coordinated structures like $[Mg(solvent)_n]^{2+}$ and $[Mg(TFSI)(X)(solvent)_n]^{+/-}$. These ratios are quantified based on the corresponding peak areas. In the positive mode, a predominant peak with an m/z of 145.6 was seen for all the electrolytes, indicating that 40–80% of Mg cations, depending on the co-anion, reside as a fully coordinated $[Mg(G2)_2]^{2+}$ complex, consistent with the findings from earlier DFT computations.[8] The prominent presence of free $TFSI^-$ in the negative mode spectrum (m/z value of 280 in Fig. 2b) confirms the well dissociation of $Mg(TFSI)_2$ in G2. The peaks at m/z 566.5 likely correspond to $[TFSI(G2)_2(H_2O)]^-$ based clusters from the base electrolyte, as evidenced by their consistent appearance across different systems. Despite this predominantly stable solvent-separated structure, the baseline electrolyte also contains 12% under-coordinated $[MgTFSI(G2)]^+$ (m/z of 438.6) and 7.3% fully coordinated $[MgTFSI(G2)_2]^+$ (m/z of 622.9). This suggests that the TFSI anion is also involved in the solvation sheath, forming a small number of contact ion pairs $[MgTFSI(solv)_n]^+$, in line with the results from Raman spectroscopy.[33] Once the second anion is added, a new peak at $m/z = 160.5$ in the positive spectra and a peak at $m/z = 649.1$ in the negative spectra appear for all three dual-salt electrolytes. The peak ($m/z = 649.1$) seems to represent a species consisting of $[Mg(TFSI)_4(G2)]^{2-}$ with its amount decreases from 19.5% with BH_4 to <1.0% with OTf. Besides, an additional peak with an m/z value of 863.9 is observed for both HMDS and OTf. This peak is indicative of undercoordinated ion pairing aggregates like $[Mg(TFSI)_3]^-$, with a substantially higher amount in OTf. These results suggest that the second anion promotes CIP formation even for TFSI itself by forcing additional TFSI into the solvation sheath. As such, the relative content of isolated $TFSI^-$ is reduced within dual-salt electrolytes, as shown in Fig. 2b and Table S1.

Table 1 The relative ratios for possible solvation species in the electrolyte calculated from the positive ESI-MS spectrum. The assigned stoichiometry provides the closest match to the observed m/z; however, a small mass discrepancy may remain. Given the known behavior of Mg–glyme–anion clusters in ESI-MS, the possible solvation species is therefore reported as a tentative assignment for each electrolyte. The $m/z \sim 170$ feature in HMDS is assigned to a mixed gas-phase fragment ion arising from concurrent fragmentation of HMDS and TFSI, involving $SiMe_3^+$- and SO_2CF_2-derived cationic fragments. This species does not represent a solution-phase coordination complex

Anions	Mass (m/z)	Possible solvation species	Ratio (%)
TFSI	145.6	$[Mg(G2)_2]^{2+}$	80.7
	438.6	$[MgTFSI(G2)]^+$	12
	622.9	$[MgTFSI(G2)_2]^+$	7.3
TFSI + BH_4	145.6	$[Mg(G2)_2]^{2+}$	52.4
	161.5	$[Mg(H_2O)_2(G2)_2]^{2+}$	7.1
	438.6	$[Mg(TFSI)(G2)]^+$	16.1
	464.3	$[Mg_3(TFSI)_2(BH_4)_2(G2)_2]^{2+}$	8.5
	585.3	$[Mg_2(TFSI)_2(G2)_4(H_2O)]^{2+}$	13.6
TFSI + HMDS	145.1	$[Mg(G2)_2]^{2+}$	72
	160.6	$[Mg(H_2O)_2(G2)_2]^{2+}$	8.1
	170.3	$[Si(CH_3)_3\text{-}SO_2CF_2]^+$	10.6
TFSI + OTf	145.1	$[Mg(G2)_2]^{2+}$	38
	160.6	$[Mg(H_2O)_2(G2)_2]^{2+}$	12.7
	280.1	$[Mg(G2)_4]^{2+}$	4.4
	307.2	$[Mg(OTf)(G2)]^+$	3.9
	441.6	$[Mg(OTf)(G2)_2]^+$	18.8
	585.3	$[Mg_2(TFSI)_2(G2)_4(H_2O)]^{2+}$	12.1
	763.1	$[Mg_2(OTf)_3(G2)_2]^+$	10.1

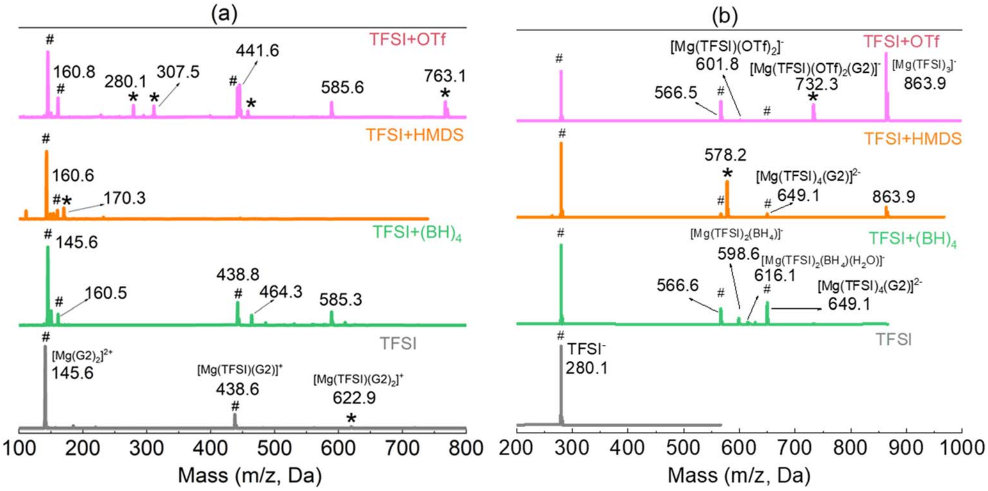

Fig. 2 ESI-MS of 0.5 M Mg^{2+} with different mixed anions (TFSI only as a baseline *vs.* TFSI + BH_4, TFSI + HMDS, and TFSI + OTf): (a) positive-mode spectra; (b) negative-mode spectra. # represents the signals common to every electrolyte. * represents the peaks specific to each electrolyte.

In the case of BH_4, four more unique peaks are observed with m/z values of 464.3 and 589.3 in the positive mode and m/z values of 598.6 and 616.6 in the negative mode, respectively. These peaks are linked to BH_4 participation in the form of $[Mg_a(TFSI)]_b(BH_4)_c(G2)_d]^{+/-}$ (Table 1). Beside, a possible coordinated structure with H_2O co-anion electrolytes (*e.g.* m/z of 161, 323, water containing structure shown in Table 1), which could confine H_2O impurities in these complexes and inhibit its activity by decreasing its concentration available at the electrode surface for interface formation. The positive spectrum for HMDS electrolyte appears clean and does not exhibit cationic complex formation at higher m/z values; instead, only the anionic species $[Mg(HMDS)_3(H_2O)_4]^-$ is observed. This is probably because $HMDS^-$ is a bulky anion with steric hindrance, making it the least effective coordinator with Mg^{2+} to form cationic species among the used anions. Upon adding OTf, the spectrum becomes more complicated compared to others. Multiple OTf-containing complexes are detected, including the cationic species $[Mg(OTf)(G2)_2]+$ and $[Mg_2(OTf)_3(G2)_2]+$, as well as the anionic cluster $[Mg(TFSI)_2(OTf)]-$. These observations indicate that both TFSI and OTf are involved in the first coordination environment of Mg^{2+}, giving rise to contact ion pairs and higher-order aggregates. Higher ratios of $[Mg(OTf)_x]^+$ formed indicate the stronger coordination ability of OTf^- relative to $TFSI^-$ likely due to its smaller steric bulk and a relatively high electronegativity, which facilitates more effective direct coordinating with Mg^{2+}, consistent with previous observations demonstrated by NMR.[34] The formation of these single anion and mixed-anion CIPs is critical, as they influence bulk properties while also stabilizing the interface by mitigating charge-transfer-induced free $TFSI^-$ decomposition,[20,35] thereby enhancing electrochemical performance (Section 2.1).

Fig. S1 presents the bulk properties of density and viscosity for each electrolyte. While density changes were minimal ($\sim$1.088 g cm^{-3}), the addition of a secondary anion primarily affected viscosity. The observed viscosity followed the order of OTf > BH_4 > HMDS, with the magnitude of relative change dependent on its coordination strength. This finding aligns with previous studies that correlate viscosity with cation–anion contact pairs.[36] The varying viscosity with different co-anions is attributed to the presence of mixed anion complexes, such as those observed with OTf^- in Fig. 2, which lead to more complex molecular and electrostatic interactions and networks within the solution. These interactions can impede the flow of the solution, thereby increasing viscosity. Additionally, consistent with previous reports,[13,15,20] mixed anion electrolytes enhance solubility compared to single-anion systems, particularly with OTf and BH_4 in diglyme, due to favorable mixed coordination with Mg^{2+} acting as "structure-breakers".[20]

2.3 Real-time interfacial speciation

The ESI-MS results demonstrate that different electroactive species are present in these electrolytes, so we expect different ion adsorption and interface formation behavior during Mg deposition. Fig. S2 shows the real-time EQCM-D spectra for the TFSI + OTf electrolyte as a representative case, highlighting three key steps. Initially, EQCM-D measurements began with the dry Pt electrode in an argon atmosphere for about 100 seconds (step 1), showing minimal changes in frequency (f) and dissipation (D), confirming the electrode's stable state as the first reference point. The electrolyte was then introduced, and EQCM signals were recorded for 600 seconds at open circuit potential (step 2), establishing a baseline frequency change as a secondary reference for electrodeposition characterization. Subsequently, the electrode was charged using either a dynamic potential scan (CV mode) or a constant current (CP mode), with frequency and dissipation changes monitored during Mg plating and stripping.

2.3.1 Electrolyte loading during OCP. A closer picture is shown in Fig. 3a illustrating the response of EQCM-D once electrolyte is injected into the cell. It is clear that electrolyte loading causes not only a significant irreversible frequency decreases, but also large increases in dissipation during step 2. The shifts in both ΔF and ΔD are electrolyte-dependent and overtone related. For example, it is evident that the change in ΔF_1 increases in the order HMDS < BH_4 < OTf < TFSI. The correlated changes in ΔF and ΔD in Fig. 3a represent the solid–liquid interactions from the attached liquid layer coupled to the neat crystal surface in contact with electrolyte. The interaction mechanisms involve both viscous coupling due to macroscopic hydrodynamic effects and surface stress due to hydrostatic pressure from the liquid phase. The viscous hydrodynamic effect is strongly dependent on electrolyte properties: their specific density (ρ) and dynamic viscosity (η), described by the Gordon–Kanazawa model (eqn (1)). Thus, from the observed change of frequency, the electrolyte properties in terms of the product of viscosity and density are calculated and compared, and the result is shown in Fig. 3b. When compared to the data obtained from bulk measurements (Fig. S1), the product of viscosity and density at the electrode interface shows lower values, although the trend remains consistent. Phenomena at the electrode interface, such as solvation layer adsorption, solvent restructuring, ion clustering, or concentration gradients, can alter the electrolyte properties (*e.g.* effective viscosity, often referred to as interfacial viscosity) locally. This interfacial viscosity can in turn affect the viscoelasticity of the double layer, charge transfer kinetics, and the (nano-scale) roughness of the deposited material. Moreover, the ratio of specific density and dynamic viscosity of a liquid defines a crucial hydrodynamic parameter, which characterizes its interaction with solids at the interface at various overtone numbers of the shear wave (n).[25,37,38] This parameter is shown in Fig. 3c, known as the penetration depth (δn, given by eqn (2) and (3)), and is important to extract the porous structure parameters of the deposited Mg solid by *in situ* hydrodynamic spectroscopy as illustrated in the following sections. The first overtone, being the lowest order, shows the greatest penetration depth, while the 13th overtone, being the highest order, has the smallest penetration depth. Interestingly, HMDS exhibits a lower penetration depth compared to the other electrolytes. But for all overtone orders n, the measured values of $\Delta f/n$ and $\Delta W/n$ form a straight line for each electrolyte, showing that they are linear functions dependent only on the penetration depth, δn, at OCP.

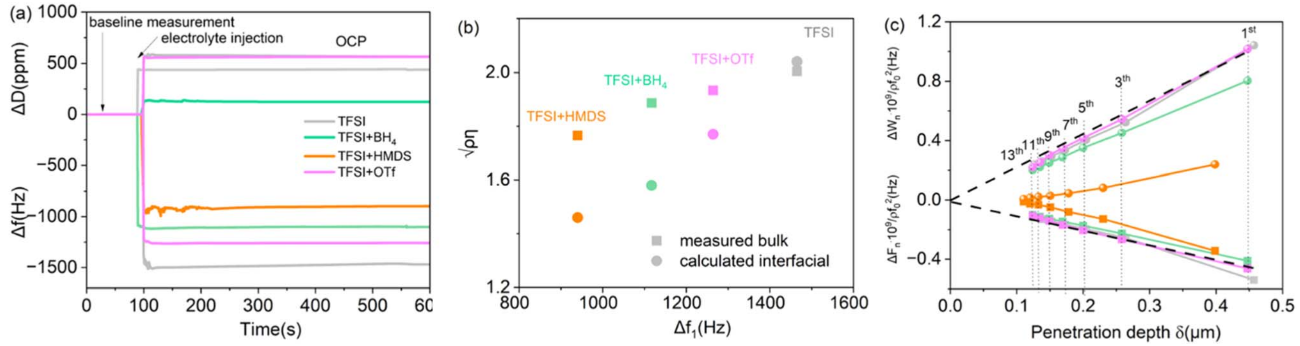

Fig. 3 (a) The magnified plot of Δ*f* and Δ*D* changes during step 1 (electrolyte loading). (b) The viscosity–density product calculated from the frequency change according to the Gordon–Kanazawa equation and compared with values from bulk measurement. (c) Normalized frequency (Δ*f*) and resonance width (Δ*W*, eqn (3)) changes for a bare Pt quartz crystal in contact with each electrolyte as a function of penetration depth determined by electrolyte viscosity-to-density ratios during OCP at 23 °C. The viscous load on a Pt electrode with an ideally flat external surface is shown as a reference (the dashed black line) which is governed by Kanazawa's equation.

2.3.2 Pre-deposition adsorption. In Fig. 4a, the different stages of metal layer plating are presented schematically alongside the corresponding EQCM-D responses from the first CV cycle. As the electrode is negatively polarized from OCP, it begins to attract and adsorb positively charged species (*e.g.*, Mg^{2+} and its associated CIPs) from the electrolyte. This pre-deposition electroadsorption occurs at potentials more positive than the bulk plating potential and is reflected by the small frequency decrease observed in the voltage window between OCP and the onset of plating (enlarged view in Fig. S3). Since no significant dissipation change was observed in this region, the adsorbed layer is likely thin and rigidly packed. The corresponding mass change on the electrode was therefore determined by fitting the frequency data to the Sauerbrey model (eqn (4)). Fig. 4b–e depict the relationship between mass change (Δm) and the quantity of charge (Q) passed on the electrode during this pre-deposition process for each electrolyte. The experimental mass per mole of electrons (mpe. eqn (5)) values for the possible surface species added to the electrode can also be determined from the slope of the Δm *vs.* ΔQ curve. The slope or the mpe value, however, is not constant over the potential sweep, revealing roughly four distinct domains for each electrolyte. The theoretical faradaic mass predicted for either neat Mg^{2+} or fully solvated $Mg(G2)^{2+}$ is also presented as references (represented by the blue and red lines, respectively, in Fig. 4b–e). The TFSI electrolyte exhibits a reduction in mass in domains I and II (from its OCP down to 0.55 V), likely due to the expulsion of already adsorbed species or desolvation from the electrode surface. Domain III (0.55 V to 0.15 V) shows no mass change, while domain IV (0.15 V to the onset plating potential of −0.27 V) sees a mass increase with an mpe value of 29 g mol^{-1}. BH_4 electrolyte shows a sharp decrease in mass in domain I (OCP to 0.54 V) and a much slower decrease in domain II (0.54 V to −0.19 V). Then, a steep mass increase is observed in domain III (−0.19 V to −0.25 V) and the average mpe value is 304 g mol^{-1}, much larger than the predicted values. For HMDS, the mass decreases slightly between OCP and 0.15 V but a positive current is observed, indicating the desorption of negatively charged larger complexes on the electrode. In the small domain II between 0.15 V and −0.1 V, mass continues to decrease. Within the domain III between 0.1 V and −0.28 V, mass starts to increase with an mpe value of 175 g mol^{-1}. For OTf containing electrolyte, between OCP and 0.38 V, the mass increases with a slope value of 138 g mol^{-1}. In the small domain II (0.38 V to 0.25 V), the mass increases with an mpe value of 47 g mol^{-1}. Domain III (0.25 V to 0.05 V) shows a further increase in mass with a smaller mpe value of 36 g mol^{-1}. When reaching the onset plating potential (∼0.23 V in domain IV), the mpe decreases to 29 g mol^{-1}, slightly larger than the predicted bare Mg^{2+} value.

The overall distinct trends in the Δm *vs.* ΔQ curves and the corresponding different mpe values for each electrolyte highlight how secondary anions significantly influence the evolving speciation at the interface. The continuously decreasing mpe values particularly with OTf indicate that local surface complexes undergo partial or complete desolvation from the G2 solvent or CIPs, along with configurational rearrangements, as they seek lower energy states near the electrode surface prior to deposition. Moreover, the substantial discrepancy between the observed mpe values and the theoretical mpe for neat Mg^{2+} reveals that the active charge carriers arriving at the interface are not bare Mg^{2+} ions, but rather partially solvated or ion-paired Mg complexes including large CIPs detected from bulk, as well as any intermediate Mg^{+} species with mass greater than 24 g mol^{-1}. These high-mass species co-adsorb onto the electrified Pt electrode interface due to electrostatic interactions, forming an ion atmosphere layer. It is important to recognize that uncharged species, such as the G2 solvent, may also participate in this process. While their involvement can lead to mass changes, their movement does not generate any electrical charge transfer; therefore, no faradaic current is associated with their motion. As such, the apparent mass change of this layer formation with potential reaching around −0.25 V increases in the order of TFSI < HMDS < BH_4 < OTf (Fig. 4f), again indicating that surface speciation adsorption behavior is influenced by interaction strength between co-anions. The results are consistent with the previous study; for example, *operando* electrochemical impedance spectroscopy (EIS) and *operando*

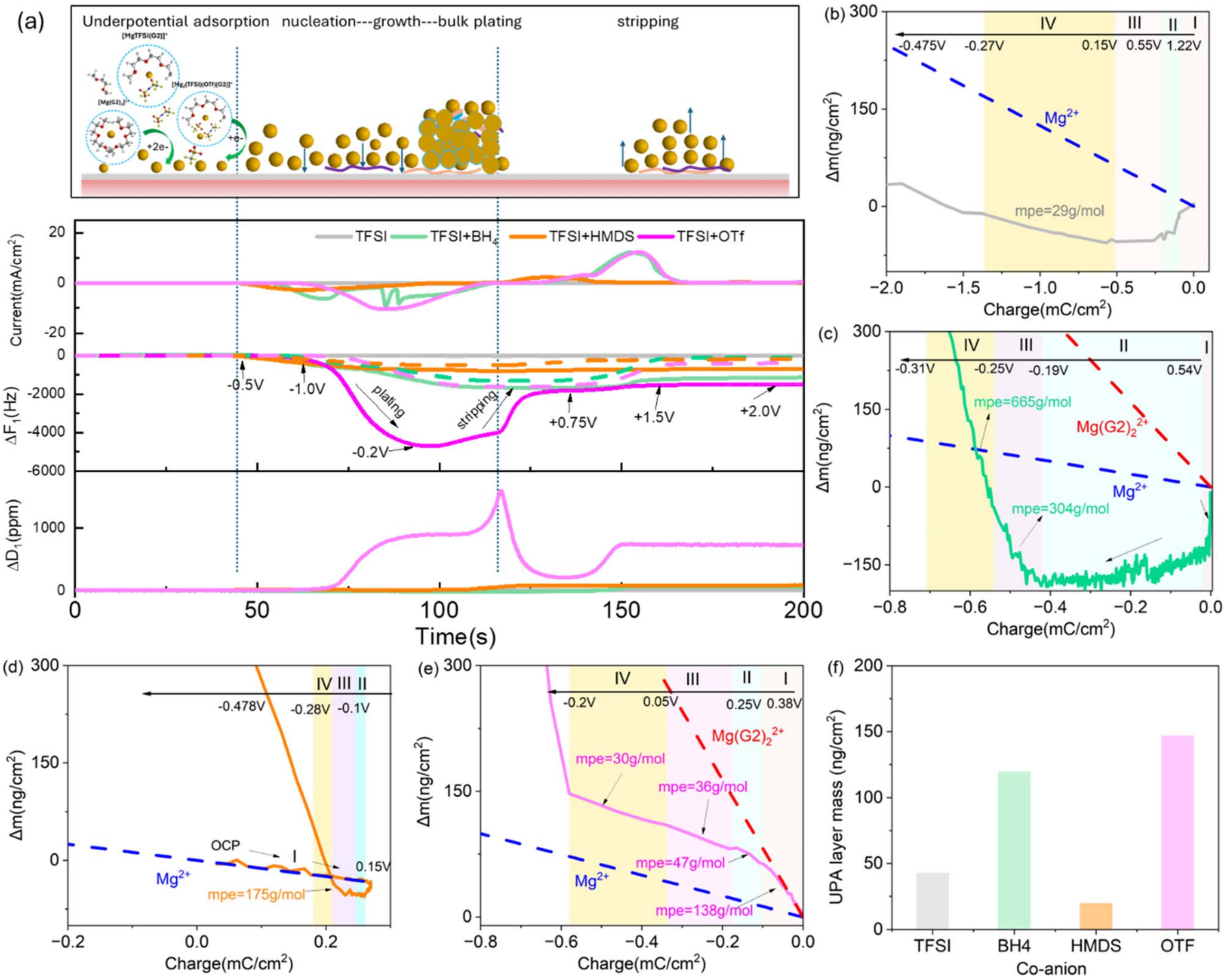

Fig. 4 (a) *In situ* EQCM-D data recorded during the first plating and stripping of Mg from different electrolytes recorded in CV mode, with the time domain (vertical dashed lines) corresponding to the different stages for metal plating in the scheme. (b)–(e) The Δmass *vs.* Δ*Q* curves for each electrolyte, correspond to voltammetric response in the potential range from OCP to the onset plating potential during the first plating process. We focus on this region because it is primarily governed by adsorption processes, assuming identical Pt surfaces in all cases. Although this is a simplified representation of a real surface, it helps explain variations in the QCM response arising from roughness modifications. (f) The adsorption surface layer mass change for each electrolyte including charged species contributing to the current and possible neutral solvent molecules as well.

electrochemical X-ray absorption spectroscopy (XAS) have shown that the BH_4 anion is involved in the interface absorption.[39] This pre-adsorption process is an initial and crucial step governing all subsequent phases of metal layer growth and bulk plating. The systematic variation of mpe values across electrolytes, together with their quantitative consistency with the CIP complexes independently identified in the bulk by ESI-MS (Table 1), establishes a direct link between bulk speciation and the charge-carrying species participating at the electrode interface. We note that the relationship between bulk ion pairing and interfacial behavior presented and discussed here is inferred through correlated, multi-modal measurements: ESI-MS for bulk speciation, EQCM-D for interfacial mass and viscoelastic dynamics, and electrochemical responses rather than direct spectroscopic observation of interfacial speciation.

2.3.3 Mg layer plating and stripping during CV. Lowering the electrode potential below the plating threshold shifts the process from simple ion adsorption to nucleation, initiating the actual formation of metal. This phase transition is dependent on the flow of current at an overpotential, which enables the formation of a stable nucleus that can ultimately progress into a thicker layer of metal. This growth is evident in the steeply rising portions of both Δ*F*–*t* and Δ*D*–*t* curves during nucleation and bulk plating (−0.25 V to −1.0 V, in Fig. 4a). Unlike the nearly unchanged TFSI baseline (implying no active Mg plating/stripping occurs), the observed frequency changes follow the order HMDS < BH4 < OTf, aligning with the trends in current behavior. When reversing the potential scan for the stripping process, the frequency increases due to the removed mass of Mg on the electrode. However, the amount of change observed during the stripping process is less than the frequency decrease during plating, mainly due to irreversible electrochemical behavior.[24] The overall plating becomes more nonuniform, creating a complicated geometric pattern of the deposit, as evident from the higher spreading between the time-dependent harmonics ($\Delta f_3/_3$, $\Delta f_5/_5$, and $\Delta f_7/_7$) and dissipation values ($\Delta D_3/_3$, $\Delta D_5/_5$, and $\Delta D_7/_7$) as cycling progresses for all the electrolytes in Fig. S2.

Thus, the Sauerbrey model is not valid in this region and a hydrodynamic model is used to retrieve the EQCM-D data.[25,37,40] By analyzing the variations in frequency (ΔF_n) and bandwidth ($\Delta W_\mathrm{n} = \Delta D_\mathrm{n} f_0$) for all overtones, we can construct the corresponding *in situ* hydrodynamic spectra. Fig. 5a–c illustrates a collection of spectra at various plating and stripping potentials (marked points in Fig. 4a) from the first cycle against penetration depth for each electrolyte. These spectra reveal distinct differences in the growth and dissolution behavior of the Mg deposits in each electrolyte. During the deposition phase (negative potentials), all systems exhibit a decrease in frequency (ΔF), corresponding to mass gain, and an increase in bandwidth (ΔW), indicating the formation of a porous and/or rough film structure. However, the magnitude of these changes varies significantly with the co-anion. The OTf system (Fig. 5c) shows the most dramatic changes, with a large increase in ΔW and a substantial drop in ΔF, signifying the growth of a highly porous or rough deposit. In contrast, the HMDS system (Fig. 5b) displays the most subdued response, with only a modest increase in ΔW, suggesting the formation of a more compact and less porous film. The BH_4^- system (Fig. 5a) shows an intermediate behavior. Upon stripping the deposited Mg at positive potentials, the bandwidth (ΔW) does not return to its initial zero value. Instead, a significant positive ΔW and a residual negative ΔF persist even at the final stripping potential of 2.0 V for all three electrolytes. This provides compelling evidence that the dissolution process is incomplete, leaving behind a persistent, porous, passivating interfacial layer on the electrode surface. This residual layer itself exhibits a hydrodynamic response (positive ΔW), confirming its porous nature. The evolution of this layer's mass and structure can be quantified by tracking the irreversible frequency change (ΔF_irrev, Fig. 5d) and residual bandwidth (ΔW_res, Fig. S4) over multiple cycles. This analysis reveals that each co-anion imparts a unique dynamic behavior to the passivation layer. The HMDS system forms the most stable passivation layer. Its irreversible frequency change (ΔF_irrev) remains nearly constant across all cycles, indicating that the passivation layer formed in the first cycle neither grows nor significantly decomposes during subsequent plating and stripping. In contrast, the layer formed with BH_4 is cumulative. Both the irreversible frequency and residual bandwidth steadily increase from cycle 1 to cycle 5, suggesting a continuous accumulation of non-strippable, porous material on the electrode surface with each cycle. The OTf^- system exhibits the most dynamic and ultimately beneficial behavior. The passivation layer initially grows from cycle 1 to 2 but is then partially "cleaned" or restructured in subsequent cycles, as shown by the decreasing ΔF_irrev from cycle 2 to 5. Critically, this dynamic layer appears to enhance subsequent redox reactions, leading to improved magnesium deposition efficiency and higher coulombic efficiencies in later cycles (Fig. 5e). These results demonstrate that

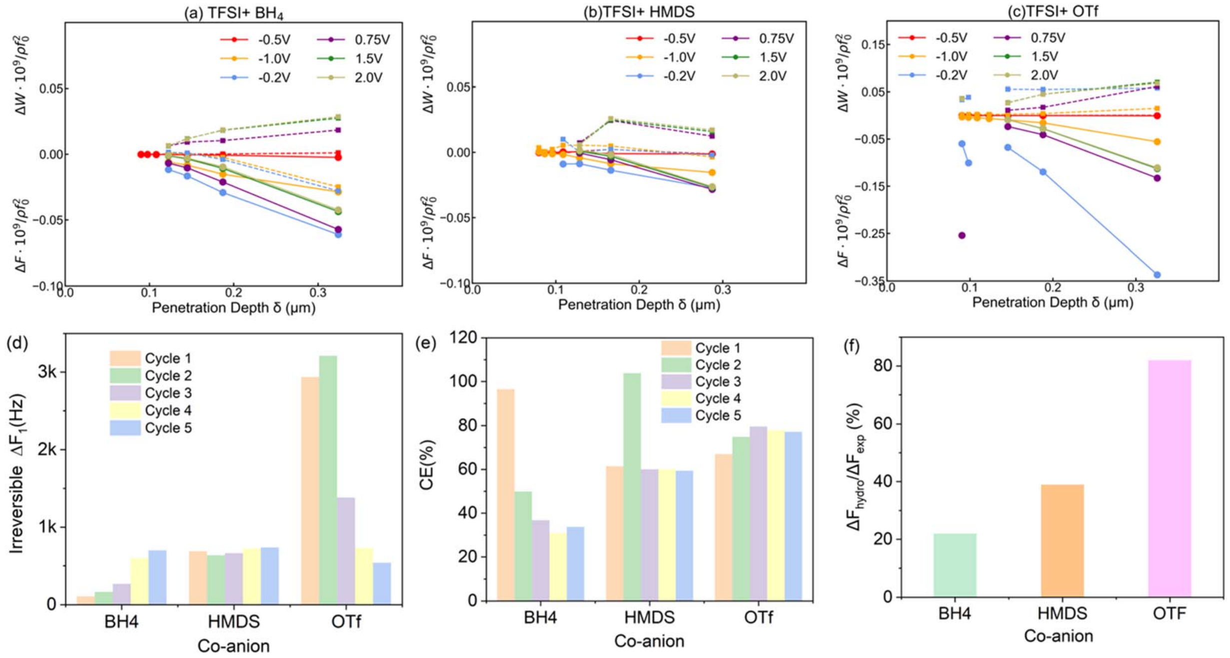

Fig. 5 (a)–(c) *In situ* hydrodynamic spectroscopy of porous Mg deposits with different mixed electrolytes retrieved from original EQCM-D spectra; the circles in the data represent changes in frequency ($\Delta F/n$) and the squares represent the change in bandwidth ($\Delta W/n$) at different plating and stripping potentials in the first cycle. (d) The irreversible frequency between plating and stripping for 5 cycles. (e) Coulombic efficiency (CE) for Mg plating for 5 cycles. (f) The hydrodynamic contribution to the total observed frequency change.

the co-anion not only dictates the initial deposit structure but also controls the stability, evolution, and even the electrochemical functionality of the residual passivation layer. This has a lasting impact on the long-term cycling performance of the electrode, as shown in Section 2.1.

The total frequency change for porous electrodeposits in contact with electrolyte is given by $\Delta F_{\exp}/n = (\Delta F/n)_{\text{solid}} + (\Delta F/n)_{\text{hydrod}}$, where $(\Delta F/n)_{\text{solid}}$ denotes the contribution from the Mg metal deposit layer and any passivation layer (*e.g.* SEI) formed on the Mg surface. $(\Delta F/n)_{\text{hydrod}}$ represents the contribution from hydrodynamic interactions between moving liquid and mesopores of deposits, which can be determined from ΔW_{n} changes. However, quantitatively separating $(\Delta F/n)_{\text{solid}}$ and $(\Delta F/n)_{\text{hydrod}}$ was difficult. The primary challenge arose from the dynamic nature of the CV experiment. During CV, the uncontrolled and varying current leads to a non-uniform deposition rate during the sweep. This promotes the growth of thick, rough Mg layers that heavily dampen the crystal, causing a loss of signal at higher harmonics ($n \geq 7$). As a result, the poor signal quality precluded a reliable fit to the full hydrodynamic model (Fig. 5a–c), preventing the precise decoupling of the solid mass from the hydrodynamic effects. Alternatively, assuming that the solid deposit including the Mg metallic layer and the passivation layer arises only from electrochemical reactions and $(\Delta F/n)_{\text{solid}} = (\Delta F/n)_{\text{theoretical}}$, the quantity $(\Delta F/n)_{\text{hydrod}}$ can also be directly estimated from the difference of $(\Delta F_{\exp}/n) - (\Delta F/n)_{\text{solid}}$ even without the explicit application of hydrodynamic models. As shown in Fig. 5f, the calculated $(\Delta F/n)_{\text{hydrod}}$ accounts for 40–80% of the total measured frequency shift depending on the co-anion and quantitatively reflects the different porous structures formed and interactions with each electrolyte due to their different properties as mentioned in 2.2 and 2.3.1.

2.3.4 Mg growth during galvanostatic plating. We next transitioned from potentiodynamic to galvanostatic (constant current) deposition to ensure a constant deposition rate and allow for a direct comparison between electrolytes using an identical amount of charge. Fig. 6a shows the cathodic chronopotentiometric curves (CP mode) and EQCM-D responses. The potential profiles for TFSI, BH4, and HMDS show two typical phases: an initial potential drop within the first 10 seconds, corresponding to Mg nucleation on the Pt electrode, followed by a gradual shift to a more positive potential until reaching a constant value for Mg growth. The TFSI baseline requires a significantly higher overpotential for nucleation and growth, around −2032 mV. For BH_4 and HMDS, the overpotentials are lower: −724 mV and −513 mV during nucleation and around −279 mV and −200 mV during growth, respectively. In contrast, the OTf profile shows a unique three-step decrease in potential over the first 150 seconds, followed by a slow increase around −320 mV for growth.

The EQCM-D profiles for Mg nucleation and growth on the Pt electrode, indicated by frequency decreases, again show distinct trends for each electrolyte. For the TFSI baseline, no significant frequency change is observed until 37 seconds, after which the frequency gently declines to approximately 10 Hz from 37 to 48 seconds, followed by a further, slower decrease over the next 550 seconds, as illustrated in the magnified graph (Fig. S5a). Each co-anion imparts a unique and distinct galvanostatic deposition profile, revealing different underlying mechanisms. In the presence of BH_4^-, a significant and immediate frequency drop occurs, indicating rapid and efficient Mg deposition from the moment the current is applied. This suggests that BH_4^- facilitates a direct and kinetically fast deposition pathway. In contrast, the electrolyte containing $HMDS^-$ exhibits a more complex, multi-stage process. An initial, slight frequency decrease over the first 10 seconds suggests the adsorption of species. This is immediately followed by a rapid frequency increase over the next 2 seconds, indicating a net desorption or removal of species from the electrode surface. Only after this initial surface rearrangement does sustained Mg deposition begin, proceeding with two distinct slopes during the subsequent growth period. The OTf^- system displays the most intricate deposition profile, characterized by several distinct stages. Initially, a slow frequency decrease occurs over the first 50 seconds, followed by a more rapid decline until 100 seconds. Notably, a frequency plateau is then observed between 100 and 150 seconds, corresponding to a potential range of −0.14 V to −0.52 V. This plateau suggests that a kinetically hindered intermediate step is required, possibly involving ionic adsorption, migration, or the need to penetrate a passivation structure before bulk deposition can proceed efficiently. Once this barrier is overcome and nucleation advances, the reduction reaction accelerates, leading to a second steep frequency drop between 150 and 190 seconds. The deposition then continues with a third, slower slope for the remainder of the 400 second period. Ultimately, the choice of co-anion dramatically impacts the total amount of deposited mass. After the full deposition period, the final frequency shifts (ΔF_1) reached −30 Hz for the baseline $TFSI^-$ electrolyte, compared to −1130 Hz for BH_4^-, −1058 Hz for $HMDS^-$, and −1258 Hz for OTf^-. This demonstrates that all three co-anions significantly enhance the overall Mg deposition efficiency compared to the $TFSI^-$-only system.

Fig. 6b illustrates the hydrodynamic spectroscopy as a function of penetration depth during the deposition step. Compared to the CV mode, all electrolytes exhibit a smaller increase in $\Delta W/n$, suggesting that the constant current mode facilitates the formation of a less porous Mg deposit. Consequently, the contribution of hydrodynamic interaction, which accounts for approximately 3% to 25% of the total frequency change, is reduced. By fitting the hydrodynamic spectra to a uniform porous layer model, two key parameters were extracted: the film thickness (h) and the permeability length (ε), which relates to pore size (Fig. 6c). The results reveal distinct structural differences among the deposits. The OTf^- system produced the thickest film ($h \approx 155$ nm), indicating the highest deposition mass, coupled with moderate permeability ($\varepsilon \approx 40$ nm). In contrast, the deposit formed with BH_4^-, while thinner ($h \approx 108$ nm), exhibited the highest permeability ($\varepsilon \approx 52$ nm), suggesting a structure with larger or more interconnected pores. The $HMDS^-$ system resulted in the thinnest ($h \approx 90$ nm) and least permeable ($\varepsilon \approx 30$ nm) film, characteristic of a denser, more compact deposit. These results quantitatively demonstrate that each co-anion directs the formation of a distinct Mg deposit/interphase with substantial differences in deposited mass and

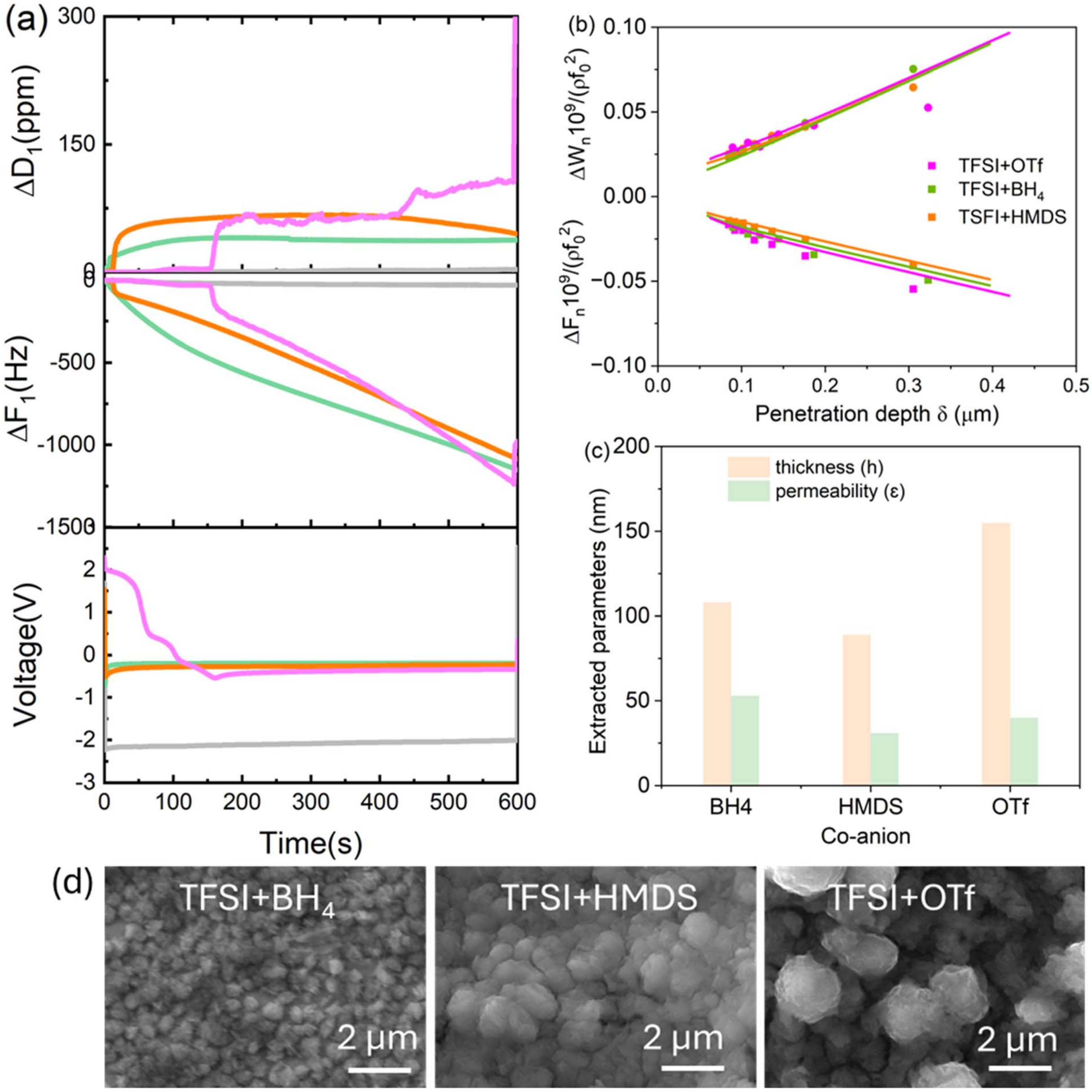

Fig. 6 (a) EQCM-D spectroscopy for the first chronopotentiometric reduction curves compared for four electrolytes. A low current density at 0.2 mA cm^{-2} was applied to produce thin deposits to avoid excessive damping on the data collection. (b) The corresponding hydrodynamic spectroscopy (dots) after 600 s deposition. The corresponding fits (lines) to the porous layer model using each viscosity and density from each electrolyte. The porous layer model is described in ref. 33. (c) The structure parameters extracted from fitting hydrodynamic spectroscopy using the porous layer model. (d) SEM images of Mg deposit morphology with mixed-anion electrolytes.

internal hydrodynamic structure. These *operando* trends are qualitatively supported by the *ex situ* SEM images in Fig. 6d. The OTf-containing electrolyte produces a more textured and extended deposit morphology, the BH_4-containing electrolyte yields a more open structure, and the HMDS-containing electrolyte results in a relatively denser and more uniform deposit. In contrast, barely any deposit particles are observed on the electrode in the baseline electrolyte (Fig. S6). Although *ex situ* microscopy does not directly capture the wet hydrodynamic structure probed by EQCM-D, these postmortem observations are broadly consistent with the *operando* interpretation of thicker, more permeable, and more compact interphases, respectively. EDS analysis further indicates that the deposited layer contains Mg together with electrolyte-derived elements such as F and S, consistent with the presence of a mixed interfacial deposit/passivation layer. This observation is also consistent with our previous XPS study of related Mg deposits, which showed only modest *ex situ* interfacial chemical differences in OTf-containing electrolytes, including slightly increased MgF-containing species.[34] Combined with the present *operando* results, this suggests that the co-anion effect is manifested strongly through dynamic interfacial and hydrodynamic behavior during deposition, rather than solely through the final surface composition. A detailed investigation of the passivation-layer chemistry and its role in governing subsequent deposition morphology and kinetics lies beyond the scope of the present work and will be addressed in future studies.

To further analyze the deposition process, frequency changes were plotted against the square root of plating time using the Cottrell equation to determine the critical time (assumed to be the time when the concentration of Mg^{2+} reaches supersaturation) by extrapolating. This is shown by the dotted straight line in Fig. S5b. Real-time EQCM monitoring demonstrated that the frequency change, corresponding to the amount of deposited Mg, increased with the square root of plating time, indicating that the diffusion of ions in the electrolyte is the rate-determining step in the Mg plating process at this current density. The determined critical time follows the order BH_4 < HMDS < OTf, with no critical time observed for the TFSI baseline. The process progresses to growth only when the applied cell voltage exceeds the critical threshold. This finding aligns with previous studies, which indicate that Mg electrodeposition is primarily a diffusion-limited process.[41,42] In the present system, this behavior likely reflects both the relatively slow transport of Mg-containing species in the electrolyte and the evolving interfacial mass/structural characteristics captured by *operando* EQCM-D during deposition.

3. Conclusions

The performance of magnesium electrodeposition is critically dependent on the electrolyte's anionic composition. In this study, we demonstrated how varying the coordination strength of a secondary anion systematically alters bulk speciation, interfacial ion adsorption, and ultimately, the Mg plating/stripping performance. We found that the anion's coordinating ability directly governs the formation of specific contact ion pairs (CIPs) in the bulk electrolyte. Importantly, this work establishes a quantitative link between bulk speciation and dynamic interface evolution. Unlike *ex situ* methods that primarily probe the final interphase, *operando* EQCM-D provides real-time, non-destructive insight into the pathways of adsorption, nucleation, growth, and stripping. These measurements show that Mg-containing ion pairs and solvated complexes shape not only the composition of the interphase, but also its mechanical character, producing anion-dependent layers that range from more permeable and solvent-coupled to more compact and rigid. These differences directly influence Mg deposition efficiency and reversibility. These insights advance our understanding of how to rationally design electrolytes using a co-anion strategy. Given the complex requirements of divalent systems, designing effective media that leverage cooperative effects by tuning anion coordination strength is essential. Future research should therefore focus on systematically exploring novel co-anions, multi-anion combinations (*e.g.*, ternary anion systems), and mixed-solvent systems to fine-tune these salt–solvent interactions for high-performance, cost-effective multivalent energy storage. Finally, the quantitative method developed in this study provides a robust analytical framework for elucidating the relationship between bulk electrolyte speciation and dynamic interface speciation. This framework advances the understanding of the chemical and mechanical properties of electrochemically active solid layers and interfaces, with broad implications for electrodeposition, battery electrodes, anticorrosion coatings, and self-organization phenomena.

4. Experimental

4.1 Electrolyte preparation

Diethylene glycol dimethyl ether (G2, 99.5%, Sigma Aldrich) was purified by vacuum distillation using a 25 cm Vigreux column over CaH_2 and stored over activated 4A molecular sieves (Sigma-Aldrich) in a glovebox prior to use. The water content in the solvent was determined to be 15 ppm by Karl Fischer titration (Mettler Toledo). All salts were vacuum-dried in the glovebox at 150 °C for 24 h before use. To ensure homogeneous solutions, the electrolytes with various combinations were stirred for a day at room temperature. All electrolyte preparation was carried out in an argon-filled glovebox (<5 ppm O_2, <1 ppm H_2O), with the mixed anion concentration consistently maintained at 0.5 M for all solutions. The density of electrolyte was measured using a density meter (Easy D40, Mettler Toledo). The viscosity of electrolyte was measured using a viscometer (Viscolab) at 23 °C.

4.2 Electrochemical cell measurement

Cyclic voltammograms and symmetric cell measurements were performed using a three-electrode PTFE Swagelok-style cell. The cell was designed with a bushing and ferrule made of polytetrafluoroethylene (PTFE) to ensure compatibility with organic solvents.[29] To minimize the effect of moisture and impurities, all glassware and sealing components were subjected to oven drying at 120 °C overnight before they were transferred to the glovebox. The working electrode for cyclic voltammetry (CV) experiments was a platinum (Pt) disk (2 mm diameter), which was cleaned with 1 M HNO_3 prior to the experiments. While freshly polished magnesium (Mg) rods served as the working and counter electrodes in Mg||Mg symmetric cells, a cutoff voltage of ± 2 V *vs.* Mg/Mg^{2+} was applied for both deposition and stripping processes. The cell assembly and electrochemical tests were performed at room temperature using a Gamry potentiostat inside an argon-filled glovebox.

4.3 Electrospray ionization-mass spectrometry (ESI-MS)

An Agilent Technologies 1260 Infinity liquid chromatograph, coupled with an Agilent 6120 Quadrupole ESI mass spectrometer (*m*/*z* values in the range of 150 to 2000), was utilized for standard mass spectrometry measurements to identify the primary speciation states and dominant ion clusters in the electrolyte. To minimize exposure to the ambient atmosphere, a direct infusion method was employed, with samples (5 μl for each electrolyte) introduced *via* airtight Hamilton syringes. The detector capillary voltage was set at 3000 V, with a flow rate for nitrogen (N_2) drying gas of 12 L min^{-1} and a nebulizer pressure of 35 psig. The drying gas temperature was maintained at 30 °C to reflect ambient solvation structures, while the fragmentor voltage was set to 70 V.

4.4 Electrochemical quartz crystal microbalance with dissipation (EQCM-D)

A quartz crystal microbalance with dissipation monitoring (QCM-D) system (Q Sense E1 module from Biolin Scientific) was utilized for multi-harmonic quartz crystal measurements inside an argon-filled glovebox. All overtone measurements, ranging from the 1st to the 13th, were obtained within a 0.3 second duration. Precise temperature control was critical, particularly when testing high-viscosity liquids. A stable temperature of 23 ± 0.1 °C in the EQCM cell was maintained because high-viscosity liquids are very sensitive to temperature fluctuations that directly impact their viscosity.

$$\Delta f_{\mathrm{n}} = -f_0^{\frac{3}{2}}\left(\frac{n\eta_l\rho_l}{\pi\mu_{\mathrm{Q}}\rho_{\mathrm{Q}}}\right)^{\frac{1}{2}} \tag{1}$$

$$\delta = \left(\frac{\eta_l}{\pi n f_0\ \rho_l}\right)^{\frac{1}{2}} \tag{2}$$

$$\Delta W_{\mathrm{n}} = \Delta D f_0 \tag{3}$$

In the Kanazawa–Gordon equation, f_0 is the nominal frequency of the dry quartz crystal (5 MHz in this study); n represents the odd overtone index $n = 1, 3, 5,\ldots$;η_{l} and ρ_{l} are the viscosity and density of the liquid electrolyte; μ_{Q} and ρ_{Q} are the shear modulus and density of the quartz crystal (2.947×10^{10} N m^{-2} and 2.648×10^3 kg m^{-3}, respectively); Δf is the measured frequency change in Hz.

$$\Delta m = -C\cdot\Delta f \tag{4}$$

The Sauerbrey equation (eqn (4)) describes the linear relationship between the added mass on the crystal and the measured frequency change and is only valid when $\Delta D = 0$. C is the Sauerbrey sensitivity factor for the crystal used (for a 5 MHz crystal, it is 18.8 ng cm^{-2} Hz).

$$\Delta f_{\mathrm{theo}} = -M_{\mathrm{w}}\frac{Q}{nFCA} \tag{5}$$

When the Sauerbrey equation is valid, M_{w} is the molar mass of the depositing species ($M_{\mathrm{w}} = 24$g mol^{-1}); Q is the integrated charge during the reduction; A is the active deposition area of the working electrode, F is Faraday's constant (96 485 coulomb mole^{-1}), and n is the number of electrons transferred to induce deposition (*i.e.* $n = 2$ for Mg deposition).

The porous layer model (eqn (6) and (7)) was used to extract hydrodynamic parameters following the approach outlined in ref. 33. In this model, the adsorbed layer is treated as a hydrodynamically permeable (porous) film characterized by three structural and geometric parameters: the permeability length ξ, which describes the penetration depth of solvent flow within the porous network; the effective layer thickness h; and the surface coverage θ, representing the fraction of the crystal surface covered by the porous layer. The auxiliary quantity $A = q_1\cosh(q_1h) + q_0\sinh(q_1h)$ relates the wavevectors in the bulk liquid (q_0) and within the porous medium (q_1) to the layer geometry. During the fitting procedure, the physical constraint $h > \xi$ was enforced to ensure that the layer thickness exceeds the hydrodynamic screening length, which is necessary for the porous medium description to remain valid. These parameters were determined for the first plating state by simultaneously fitting the model to the frequency and dissipation shifts across multiple overtones.

$$\begin{aligned}\Delta f_{\mathrm{n}} = -\theta\frac{2f_0{}^2\rho}{\sqrt{\mu_{\mathrm{q}}\rho_{\mathrm{q}}}}\mathrm{Re}\Bigg\{&\frac{1}{q_0} + \frac{h}{\varepsilon^2 q_1{}^2} - \frac{1}{A}\frac{1}{\varepsilon^2 q_1{}^2}\Bigg[\frac{2q_0}{q_1}[\cosh(q_1h - 1)]\\ &+ \sinh(q_1h)\Bigg] - (1-\theta)\frac{2f_0{}^2\rho}{\sqrt{\mu_{\mathrm{q}}\rho_{\mathrm{q}}}}\mathrm{Re}\left(\frac{1}{q_0}\right)\Bigg\}\end{aligned} \tag{6}$$

$$\begin{aligned}\Delta W_{\mathrm{n}} = -\theta\frac{4f_0{}^2\rho}{\sqrt{\mu_{\mathrm{q}}\rho_{\mathrm{q}}}}I\Bigg\{&\frac{1}{q_0} + \frac{h}{\varepsilon^2 q_1{}^2} - \frac{1}{A}\frac{1}{\varepsilon^2 q_1{}^2}\Bigg[\frac{2q_0}{q_1}[\cosh(q_1h - 1)]\\ &+ \sinh(q_1h)\Bigg] - (1-\theta)\frac{4f_0{}^2\rho}{\sqrt{\mu_{\mathrm{q}}\rho_{\mathrm{q}}}}\mathrm{Im}\left(\frac{1}{q_0}\right)\Bigg\}\end{aligned} \tag{7}$$

Author contributions

Zhenzhen Yang: conceptualization, methodology, investigation, validation, resources, writing – original draft, and visualization. Stefan Illic: investigation and resources. Qian Liu: resources. Chen Liao: resources and writing – review and editing. Trahey Lynn: funding acquisition. Brian Ingram: writing – review and editing, supervision, project administration, and funding acquisition.

Conflicts of interest

There are no conflicts of interest to declare.

Data availability

The data and python scripts used for the fitting procedure that support the findings of this study are available from the corresponding author upon reasonable request.

Supplementary information (SI): *in situ* EQCM-D measurements during OCP monitoring; *in situ* EQCM-D measurement during the first negative scan in CV measurements from 300–460 s; table of the molecular mass for possible solvated species; CV data of the first 3 cycles. See DOI: https://doi.org/10.1039/d6ta02098d.

Acknowledgements

The collection and investigation of experimental data were supported by the Joint Center for Energy Storage Research

(JCESR), an Energy Innovation Hub funded by the U.S. Department of Energy, Office of Science, Basic Energy Sciences. The final data collection and manuscript preparation were further supported by the Center for Steel Electrification by Electrosynthesis (C-STEEL), an Energy Earthshot Research Center funded by the U.S. Department of Energy, Office of Science, Basic Energy Sciences (BES) and Advanced Scientific Computing Research (ASCR), under contract no. DE-AC02-06CH11357.

References

1 R. Deivanayagam, B. J. Ingram and R. Shahbazian-Yassar, Progress in Development of Electrolytes for Magnesium Batteries, *Energy Storage Mater.*, 2019, **21**, 136–153.

2 R. Mohtadi, O. Tutusaus, T. S. Arthur, Z. Zhao-Karger and M. Fichtner, The Metamorphosis of Rechargeable Magnesium Batteries, *Joule*, 2021, **5**(3), 581–617.

3 J. Zheng and L. A. Archer, Controlling Electrochemical Growth of Metallic Zinc Electrodes: Toward Affordable Rechargeable Energy Storage Systems, *Sci. Adv.*, 2021, **7**(2), eabe0219.

4 J. K. Yadav, B. Rani, P. Saini and A. Dixit, Rechargeable Iron-Ion (Fe-Ion) Batteries: Recent Progress, Challenges, and Perspectives, *Energy Adv.*, 2024, **3**(5), 927–944.

5 Z. Li, J. Yu and X. Liu, Materials and Devices for Iron Batteries: Recent Progress and Perspectives, *ACS Appl. Energy Mater.*, 2025, **8**(14), 9965–9982.

6 A. Taghavi-Kahagh, H. Roghani-Mamaqani and M. Salami-Kalajahi, Powering the Future: A Comprehensive Review on Calcium-Ion Batteries, *J. Energy Chem.*, 2024, **90**, 77–97.

7 Y. Chen, K. Fan, Y. Gao and C. Wang, Challenges and Perspectives of Organic Multivalent Metal-Ion Batteries, *Adv. Mater.*, 2022, **34**(52), 2200662.

8 N. N. Rajput, T. J. Seguin, B. M. Wood, X. Qu and K. A. Persson, Elucidating Solvation Structures for Rational Design of Multivalent Electrolytes—a Review, *Top. Curr. Chem.*, 2018, **376**(3), 19.

9 X. Chen, X. Q. Zhang, H. R. Li and Q. Zhang, Cation–Solvent, Cation–Anion, and Solvent–Solvent Interactions with Electrolyte Solvation in Lithium Batteries, *Batteries Supercaps*, 2019, **2**(2), 128–131.

10 J. Han, A. Mariani, S. Passerini and A. Varzi, A Perspective on the Role of Anions in Highly Concentrated Aqueous Electrolytes, *Energy Environ. Sci.*, 2023, **16**(4), 1480–1501.

11 M. Salama, I. Shterenberg, H. Gizbar, N. N. Eliaz, M. Kosa, K. Keinan-Adamsky, M. Afri, L. J. W. Shimon, H. E. Gottlieb, D. T. Major, Y. Gofer and D. Aurbach, Unique Behavior of Dimethoxyethane (Dme)/Mg(N(So2cf3)2)2 Solutions, *J. Phys. Chem. C*, 2016, **120**(35), 19586–19594.

12 D. M. Driscoll, S. N. Lavan, M. Zorko, P. C. Redfern, S. Ilic, G. Agarwal, T. T. Fister, R. S. Assary, L. Cheng, D. Strmcnik, M. Balasubramanian and J. G. Connell, Emergent Solvation Phenomena in Non-Aqueous Electrolytes with Multiple Anions, *Chem*, 2023, **9**(7), 1955–1971.

13 D.-T. Nguyen, A. Y. S. Eng, R. Horia, Z. Sofer, A. D. Handoko, M.-F. Ng and Z. W. Seh, Rechargeable Magnesium Batteries Enabled by Conventional Electrolytes with Multifunctional Organic Chloride Additives, *Energy Storage Mater.*, 2022, **45**, 1120–1132.

14 D. Chinnadurai, W. Y. Lieu, S. Kumar, G. Yang, Y. Li and Z. W. Seh, A Passivation-Free Solid Electrolyte Interface Regulated by Magnesium Bromide Additive for Highly Reversible Magnesium Batteries, *Nano Lett.*, 2023, **23**(4), 1564–1572.

15 D.-T. Nguyen, A. Y. S. Eng, M.-F. Ng, V. Kumar, Z. Sofer, A. D. Handoko, G. S. Subramanian and Z. W. Seh, A High-Performance Magnesium Triflate-Based Electrolyte for Rechargeable Magnesium Batteries, *Cell Rep. Phys. Sci.*, 2020, **1**(12), 100265.

16 A. M. Melemed, D. A. Skiba and B. M. Gallant, Toggling Calcium Plating Activity and Reversibility through Modulation of Ca2+ Speciation in Borohydride-Based Electrolytes, *J. Phys. Chem. C*, 2022, **126**, 892–902.

17 Y. Shao, T. Liu, G. Li, M. Gu, Z. Nie, M. Engelhard, J. Xiao, D. Lv, C. Wang, J.-G. Zhang and J. Liu, Coordination Chemistry in Magnesium Battery Electrolytes: How Ligands Affect Their Performance, *Sci. Rep.*, 2013, **3**(1), 3130.

18 D. Samuel, C. Steinhauser, J. G. Smith, A. Kaufman, M. D. Radin, J. Naruse, H. Hiramatsu and D. J. Siegel, Ion Pairing and Diffusion in Magnesium Electrolytes Based on Magnesium Borohydride, *ACS Appl. Mater. Interfaces*, 2017, **9**(50), 43755–43766.

19 D. Chinnadurai, Y. Li, C. Zhang, G. Yang, W. Y. Lieu, S. Kumar, Z. Xing, W. Liu and Z. W. Seh, Chloride-Free Electrolyte Based on Tetrabutylammonium Triflate Additive for Extended Anodic Stability in Magnesium Batteries, *Nano Lett.*, 2023, **23**(23), 11233–11242.

20 S. Ilic, S. N. Lavan, N. J. Leon, H. Liu, A. Jain, B. Key, R. S. Assary, C. Liao and J. G. Connell, Mixed-Anion Contact Ion-Pair Formation Enabling Improved Performance of Halide-Free Mg-Ion Electrolytes, *ACS Appl. Mater. Interfaces*, 2024, **16**(1), 435–443.

21 C. Liao, N. Sa, B. Key, A. K. Burrell, L. Cheng, L. A. Curtiss, J. T. Vaughey, J.-J. Woo, L. Hu, B. Pan and Z. Zhang, The Unexpected Discovery of the Mg(Hmds)2/Mgcl2 Complex as a Magnesium Electrolyte for Rechargeable Magnesium Batteries, *J. Mater. Chem. A*, 2015, **3**(11), 6082–6087.

22 Z. Yang, M. C. Dixon, R. A. Erck and L. Trahey, Quantification of the Mass and Viscoelasticity of Interfacial Films on Tin Anodes Using Eqcm-D, *ACS Appl. Mater. Interfaces*, 2015, **7**(48), 26585–26594.

23 B. W. Schick, X. Hou, V. Vanoppen, M. Uhl, M. Kruck, E. J. Berg and T. Jacob, Revealing the Structural Evolution of Electrode/Electrolyte Interphase Formation During Magnesium Plating and Stripping with Operando Eqcm-D, *ChemSusChem*, 2024, **17**(4), e202301269.

24 Z. Yang, N. J. Leon, C. Liao, B. J. Ingram and L. Trahey, Effect of Salt Concentration on the Interfacial Solvation Structure and Early Stage of Solid–Electrolyte Interphase Formation in Ca(Bh4)2/Thf for Ca Batteries, *ACS Appl. Mater. Interfaces*, 2023, **15**(20), 25018–25028.

25 S. Sigalov, N. Shpigel, M. D. Levi, M. Feldberg, L. Daikhin and D. Aurbach, Electrochemical Quartz Crystal Microbalance with Dissipation Real-Time Hydrodynamic Spectroscopy of Porous Solids in Contact with Liquids, *Anal. Chem.*, 2016, **88**(20), 10151–10157.

26 V. Vanoppen, D. Johannsmann, X. Hou, J. Sjölund, P. Broqvist and E. J. Berg, Exploring Metal Electroplating for Energy Storage by Quartz Crystal Microbalance: A Review, *Adv. Sens. Res.*, 2024, **3**(9), 2400025.

27 J. G. Connell, M. Zorko, G. Agarwal, M. Yang, C. Liao, R. S. Assary, D. Strmcnik and N. M. Markovic, Anion Association Strength as a Unifying Descriptor for the Reversibility of Divalent Metal Deposition in Nonaqueous Electrolytes, *ACS Appl. Mater. Interfaces*, 2020, **12**(32), 36137–36147.

28 D. Aurbach, H. Gizbar, A. Schechter, O. Chusid, H. E. Gottlieb, Y. Gofer and I. Goldberg, Electrolyte Solutions for Rechargeable Magnesium Batteries Based on Organomagnesium Chloroaluminate Complexes, *J. Electrochem. Soc.*, 2002, **149**(2), A115.

29 Z. Yang, M. Yang, N. T. Hahn, J. Connell, I. Bloom, C. Liao, B. J. Ingram and L. Trahey, Toward Practical Issues: Identification and Mitigation of the Impurity Effect in Glyme Solvents on the Reversibility of Mg Plating/Stripping in Mg Batteries, *Front. Chem.*, 2022, **10**, 966332.

30 H. Kuwata, M. Matsui and N. Imanishi, Passivation Layer Formation of Magnesium Metal Negative Electrodes for Rechargeable Magnesium Batteries, *J. Electrochem. Soc.*, 2017, **164**(13), A3229.

31 L. Zhang, Y. Liu, X. Wang, Z. Cui, C. Xiao, C. Chen, J. Wang, G. Huang, D. Zhang and F. Pan, Deciphering the Interfacial Electrochemistry of Non-Nucleophilic Mg(Tfsi)2 as 4 v-Class Electrolyte for Mg Batteries, *Chem. Eng. J.*, 2025, **516**, 162410.

32 J. Zhang, J. Liu, M. Wang, Z. Zhang, Z. Zhou, X. Chen, A. Du, S. Dong, Z. Li, G. Li and G. Cui, The Origin of Anode–Electrolyte Interfacial Passivation in Rechargeable Mg-Metal Batteries, *Energy Environ. Sci.*, 2023, **16**(3), 1111–1124.

33 Z. Yang, L. Gao, N. J. Leon, C. Liao, B. J. Ingram and L. Trahey, Quantifying the Correlation between Coordination Chemistry, Interfacial Formation, and Electrochemical Performances for Mg Battery Electrolytes, *ACS Appl. Energy Mater.*, 2024, **7**(4), 1666–1675.

34 S. Ilic, S. N. Lavan, N. J. Leon, H. Liu, A. Jain, B. Key, R. S. Assary, C. Liao and J. G. Connell, Mixed-Anion Contact Ion-Pair Formation Enabling Improved Performance of Halide-Free Mg-Ion Electrolytes, *ACS Appl. Mater. Interfaces*, 2024, **16**(1), 435–443.

35 V. Prabhakaran, G. Agarwal, J. D. Howard, S. Wi, V. Shutthanandan, D.-T. Nguyen, L. Soule, G. E. Johnson, Y.-S. Liu, F. Yang, X. Feng, J. Guo, K. Hankins, L. A. Curtiss, K. T. Mueller, R. S. Assary and V. Murugesan, Coordination-Dependent Chemical Reactivity of Tfsi Anions at a Mg Metal Interface, *ACS Appl. Mater. Interfaces*, 2023, **15**(5), 7518–7528.

36 H. Peng and A. V. Nguyen, A Link between Viscosity and Cation-Anion Contact Pairs: Adventure on the Concept of Structure-Making/Breaking for Concentrated Salt Solutions, *J. Mol. Liq.*, 2018, **263**, 109–117.

37 M. D. Levi, N. Shpigel, S. Sigalov, V. Dargel, L. Daikhin and D. Aurbach, In Situ Porous Structure Characterization of Electrodes for Energy Storage and Conversion by Eqcm-D: A Review, *Electrochim. Acta*, 2017, **232**, 271–284.

38 N. Shpigel, M. D. Levi, S. Sigalov, O. Girshevitz, D. Aurbach, L. Daikhin, P. Pikma, M. Marandi, A. Jänes, E. Lust, N. Jäckel and V. Presser, In Situ Hydrodynamic Spectroscopy for Structure Characterization of Porous Energy Storage electrodes, *Nat. Mater.*, 2016, **15**(5), 570–575.

39 H. Wang, X. Feng, Y. Chen, Y.-S. Liu, K. S. Han, M. Zhou, M. H. Engelhard, V. Murugesan, R. S. Assary, T. L. Liu, W. Henderson, Z. Nie, M. Gu, J. Xiao, C. Wang, K. Persson, D. Mei, J.-G. Zhang, K. T. Mueller, J. Guo, K. Zavadil, Y. Shao and J. Liu, Reversible Electrochemical Interface of Mg Metal and Conventional Electrolyte Enabled by Intermediate Adsorption, *ACS Energy Lett.*, 2020, **5**(1), 200–206.

40 B. W. Schick, V. Vanoppen, M. Uhl, M. Kruck, S. Riedel, Z. Zhao-Karger, E. J. Berg, X. Hou and T. Jacob, Influence of Chloride and Electrolyte Stability on Passivation Layer Evolution at the Negative Electrode of Mg Batteries Revealed by Operando Eqcm-D, *Angew. Chem., Int. Ed.*, 2024, **63**(52), e202413058.

41 V. Attari, S. Banerjee and R. Arroyave, On the Kinetics of Electrodeposition in a Magnesium Metal Anode, *Acta Mater.*, 2024, **276**, 120089.

42 J. Eaves-Rathert, K. Moyer, M. Zohair and C. L. Pint, Kinetic-Versus Diffusion-Driven Three-Dimensional Growth in Magnesium Metal Battery Anodes, *Joule*, 2020, **4**(6), 1324–1336.